Applied Ocean Research 138 (2023) 103621

Contents lists available at ScienceDirect

Applied Ocean Research

journal homepage: www.elsevier.com/locate/apor

Invited paper

A numerical investigation on three-dimensional swirling instability in viscous sloshing flows

C. Pilloton [a], J. Michel [a], A. Colagrossi [a,b,*], S. Marrone [a]

[a] CNR-INM, Institute of marine engineering, Rome, 00128, Italy
[b] ECN/CNRS, Ecole Centrale Nantes, LHEEA Lab., 1 rue de la Noe Nantes, 44300, France

ARTICLE INFO

Keywords:
Swirling instability
Sloshing flows
Smoothed particle hydrodynamics (SPH)
Viscous flows
Free-surface flows

ABSTRACT

Resonant three-dimensional nonlinear sloshing in a square-base basin is analysed numerically to investigate swirling instability. The aim of this research is based on understanding how viscosity influences this instability. Four different fluids at increasing Reynolds number were considered in a tank forced to oscillate in a horizontal motion. The present study investigates the tight relation between the energy dissipation and this instability, showing that water tends to dissipate more energy during its rotating motion than the other three liquids characterised by higher viscosity. This aspect is strictly linked to the occurrence of free-surface fragmentation and liquid impacts. The numerical solutions are provided using an enhanced version of the Smoothed Particle Hydrodynamics (SPH) model called δ-LES-SPH model which proved to be suitable for the simulation of violent free-surface flows.

1. Introduction

Sloshing flow phenomena may appear in partially filled tanks produced by the motion of vehicles as ships, aircraft, spacecrafts, rockets and satellites, or in containers as a consequence of earthquakes. In turn, the raising of internal waves may cause impact loads, influencing the vehicle's motion and the structure dynamics in their mutual interaction. In the last decades, sloshing flows have been widely investigated with analytical, experimental and numerical methods.

Sloshing phenomena are deeply analysed in the book by Faltinsen and Timokha (2009), where a particular attention is referred to the land-based and marine applications focusing on ship tanks. Although three-dimensional flow studies are not widespread in the literature, it is well known that the fluid can evolve in plane waves, rotational motion or in a chaotic solution, depending on the tank aspect ratio, the filling height, the oscillation frequency and the direction of the forced motion. In particular, when sloshing waves move in a clockwise or counterclockwise direction along the tank walls, this kind of motion is called "swirling" and it is a special feature of 3D sloshing flow that may take place in vertical cylinder, spherical, square-base or nearly square-base tanks when they oscillate with a forcing frequencies near to the resonant one.

A weakly nonlinear analysis via multiple timescale method was developed by Bongarzone et al. (2022) to describe the resonant sloshing response in a circular cylinder to longitudinal force. That analysis was confirmed by a dedicated experimental campaign which focused on the study of the most relevant secondary super-harmonic resonance. Three possible regimes were identified: stable planar double crest waves, irregular motion and stable swirling double crest waves. The free surface response in a cylindrical tank subjected to an elliptic periodic orbit was investigated by Marcotte et al. (2023). The existence of a frequency range where stable swirling can be either co- or counter-directed with respect to the tank's direction of motion is experimentally analysed and numerically predicted with an inviscid asymptotic model and the addition of heuristic damping.

Sloshing in a circular cylinder with a slowly rotating liquid has been experimentally and theoretically investigated in Tsarau et al. (2021) for aquaculture fish farms. In particular it is shown that liquid rotation is able to modify the sloshing resonant regimes and for some specific conditions the unwanted swirling instability can be suppressed. An intense examination of resonant three-dimensional nonlinear sloshing in a square-base basin with finite depth is studied theoretically with a developed approximate (asymptotic) Narimanov–Moiseev-type multi-modal theory and compared with experimental results in Faltinsen et al. (2003, 2005b, 2006), Faltinsen and Timokha (2017), Faltinsen et al. (2020). In particular, in Faltinsen et al. (2003) the theoretical part is focused on periodic solutions of the modal system with longitudinal and diagonal excitations. Three types of solutions are found for each case: 'planar'/'diagonal', 'swirling' waves and 'square'-like resonant standing waves. In Faltinsen et al. (2005b) a more accurate investigation of the strong nonlinear amplification of higher modes is performed and the

* Corresponding author at: CNR-INM, Institute of marine engineering, Rome, 00128, Italy.
E-mail address: andrea.colagrossi@cnr.it (A. Colagrossi).

https://doi.org/10.1016/j.apor.2023.103621
Received 20 March 2023; Received in revised form 12 May 2023; Accepted 1 June 2023

effective frequency domains of the secondary resonance are quantified. A parametric analysis based on the size of the tank shows in Faltinsen et al. (2006) that the frequency domains, where the wave regimes are defined, are strongly sensitive to breadth/width ratio also with small perturbations around 1. Qualitative and quantitative studies are performed in Faltinsen and Timokha (2017) using the modal theory from Faltinsen et al. (2003) equipped with the linear damping terms. Finally, further finalisation of the case studies is performed in Faltinsen et al. (2020) by considering the non-parametric three-dimensional cyclic movements of the tank combining sway, pitch, surge, roll and yaw.

In Jin et al. (2020) the effect of viscosity was investigated experimentally in sloshing flows in intermediate liquid depth. The free-surface profiles of low and high viscous fluids under resonant excitation are analysed in connection with the dynamic pressures and excitation accelerations. In Wu and Chen (2009) and Chen and Wu (2011), a 3D time-independent inviscid Finite Difference Method (FDM) is developed to simulate sloshing waves in a three-dimensional square base tank. Surge and sway excitation motions are coupled with various excitation angles under a wide range of tank motion frequencies and with an arbitrary depth. The authors observed five types of sloshing waves that are strictly connected with the excitation frequency and swirling wave pattern appears when the tank is forced with a frequency near to the first fundamental mode. In Wu et al. (2013), the results of the same time-independent finite difference numerical model were compared with measures from an experimental campaign where a detailed analysis of sloshing-induced hydrodynamic force resulting from different types of sloshing waves are presented. In the work of Chen et al. (2023) the mechanism of swirling waves direction is investigated numerically and experimentally through the evolution of the hydrodynamic force of a three-dimensional tank under a nearly-resonant excitation with oblique excitation angle. Furthermore, the mechanism of the switch of the swirling direction is claimed to occur at the peak and through the envelope of the time-history of the vertical force. A further numerical investigation on a squared tank forced with a coupled surge-sway motion under various oblique excitation angles and water depths was made by Wu et al. (2023), studying in depth the evolution of swirling waves during the initial transient stage in terms of kinematic, dynamic and energy characteristics of sloshing waves. The mechanism of the swirling phenomenon is still not clear but its evolution seems to be very sensitive to the physical conditions such as tank geometry, the filling height, the excitation frequency, the amplitude and the angle of the external forcing. Regarding the simulation of 3D nonlinear sloshing using Navier–Stokes equations, in Liu and Lin (2008) a Finite Volume Method combined with a Volume of Fluid (VOF) algorithm and a large-eddy turbulence model was developed to study violent sloshing flows with breaking waves and liquid fragmentation.

The present work is dedicated to the analysis of how swirling instability is influenced by the fluid viscosity. This aspect was rarely addressed in the literature. Furthermore, the energy damping associated with the onset of the swirling regime is studied in detail, showing that when the swirling instability is excited the slosh dissipation significantly increases. For this purpose, four different fluids inside a square-base 3D tank are considered with a filling ratio of 50.8%. The tank is forced horizontally along one of the tank edges at the first resonant frequency. The liquids considered are water, sunflower oil, castor oil and glycerine and the associated Reynolds numbers range from 214.8 up to 253,100, covering four orders of magnitude. As expected when increasing the viscosity the swirling instability is delayed in time, and specifically we found that when using the glycerine the swirling mode is completely suppressed, at least in the considered time range.

In addition, the highest slosh dissipation is obtained with liquids characterised by lower viscosity, confirming the conclusions drawn in other sloshing studies. For example in Bouscasse et al. (2014a,b) the authors found that the damping of a driven pendulum filled with liquid is higher when water is used with respect to sunflower oil or glycerin. An analogous conclusion is described in Calderon-Sanchez et al. (2023, 2021) where a sloshing rig moving vertically on a mechanical guide with a tank attached to a set of six springs is studied using different liquids; again when less viscous liquids are used the damping of its motion is higher. This is linked with the fragmentation phenomena occurring at higher Reynolds numbers which induce a larger energy dissipation.

The numerical simulation performed with water refers to an experiment described in Faltinsen et al. (2005a), where the swirling instability is excited choosing a horizontal periodical motion with a frequency that is close to the lowest natural frequency. In the present work the phenomena is studied through numerical simulations with Smoothed Particle Hydrodynamics (SPH). Thanks to the conservation properties of the SPH, this numerical method is particularly suitable for simulating long-time evolution (Pilloton et al., 2022). In particular in this work an enhanced model called δ-LES-SPH is adopted. The latter has been demonstrated to be suitable for the simulation of violent sloshing flow see *e.g.* (Marrone et al., 2021a; Michel et al., 2022; Malan et al., 2022).

The article is organised as follows. Section 2 introduces the governing equations and the δ-LES-SPH model is briefly recalled. The evaluation of the slosh dissipation is linked to phase lag between the tank and the liquid centre of mass motions. Section 3 is devoted to introduce the test-case simulated varying the fluid inside the 3D square-base tank. Numerical results are presented, underling the effects of fluid viscosity and the dissipation process. In particular, we will show how the different viscosity of the fluids produces a different resonant behaviour supported through the comparison of the free-surface configurations, time histories of the mechanical energy and orbital evolution of the horizontal force components.

2. Model retained and its numerical approximation

2.1. Governing equations

The governing equation used for modelling the sloshing flow in the present work are the Navier–Stokes equations. Only the liquid phase is modelled, thermal conductivity and surface tension can be neglected for the specific problem at hand. Furthermore, the liquid is assumed to be a weakly compressible medium. The tank is assumed to translate along the x-axis. The equation are formulated in the non-inertial frame of reference (Ni-FoR). With these assumptions, the flow evolution is governed by:

$$\begin{cases} \dfrac{D\rho}{Dt} = -\rho\,\mathrm{div}(\boldsymbol{u}), & \rho\dfrac{D\boldsymbol{u}}{Dt} = \mathrm{div}(\mathbb{T}) + \rho\boldsymbol{g} - \rho a_{tank}(t)\,\boldsymbol{i} \\ \dfrac{De}{Dt} = \dfrac{\mathbb{T}:\mathbb{D}}{\rho}, & \dfrac{D\boldsymbol{r}}{Dt} = \boldsymbol{u}, \qquad p = f(\rho) \end{cases} \tag{1}$$

where D/Dt represents the Lagrangian derivative, $\boldsymbol{u}$ the fluid velocity, ρ the liquid density, $\boldsymbol{g}$ the gravitational acceleration, $a_{tank}(t)$ the tank acceleration, $\boldsymbol{i}$ the unit vector of the x-axis, $\mathbb{T}$ the stress tensor, e the specific internal energy, $\mathbb{D}$ the rate of stress tensor and $\boldsymbol{r}$ the position of material point.

The liquid is assumed to be Newtonian and the flow isothermal *i.e*: $\mathbb{T} = [-p + \lambda\,\mathrm{div}(\boldsymbol{u})]\,\mathbb{I} + 2\,\mu\,\mathbb{D}$, where μ and λ are the primary and secondary dynamic viscosity of the liquid and $\mathbb{I}$ is the identity tensor. The liquid is assumed also as barotropic and therefore the pressure depends on the density exclusively. As a consequence the internal energy equation in (1) is decoupled by the momentum equation and it is used just to control the energy conservation of the numerical scheme.

The assumption of small density variations allows for using a linear equation of state

$$p = c_0^2\left(\rho - \rho_0\right)$$

where ρ_0 is the density at the free surface and c_0 is the speed of sound. By considering that the time integration is performed with a time step

related to the value of c_0, the latter is always set lower than its physical counterpart (in the present work, about two orders of magnitude lower). The weakly-compressible regime is always guaranteed by the condition:

$$c_0 \geq 10 \max\left(U_{max}, \sqrt{(\Delta p)_{max}/\rho} \right), \tag{2}$$

where U_{max} and $(\Delta p)_{max}$ stand respectively for the expected maximum velocity and pressure variation within the fluid domain.

2.2. The δ-LES-SPH scheme

Following Marrone et al. (2021b), Michel et al. (2022), Malan et al. (2022) in the present work the δ-LES-SPH scheme derived in Antuono et al. (2021a), Meringolo et al. (2019) is used to approximate Eq. (1). The main characteristics of the scheme are recalled here and for specifics the interested reader is referred to the above-mentioned articles. In order to recover regular spatial distribution of particles and consequently accurate approximation of the SPH operators (Quinlan et al., 2006; Nestor et al., 2009), a Particle Shifting Technique (PST) is used (see also *e.g.* Lind et al., 2012). For the sake of brevity the specific law adopted for the shifting velocity $\delta\boldsymbol{u}$ is not reported here, this being identical to the one adopted by Marrone et al. (2021b), Michel et al. (2022) in which violent sloshing problems were studied.

This PST velocity is then taken into account within the continuity and momentum equations by rewriting the governing equations (1) in an Arbitrary-Lagrangian–Eulerian (ALE) framework. To this purpose a quasi-Lagrangian derivative

$$\frac{d(\bullet)}{dt} := \frac{\partial(\bullet)}{\partial t} + \nabla(\bullet)\cdot(\boldsymbol{u}+\delta\boldsymbol{u})$$

is used and the SPH schemes reads as:

$$\begin{cases} \dfrac{\mathrm{d}\rho_i}{\mathrm{d}t} &= -\rho_i \,\mathrm{div}(\boldsymbol{u}_i) - \rho_i \,\mathrm{div}(\delta\boldsymbol{u}_i) + \mathrm{div}(\rho_i \delta\boldsymbol{u}_i) + \mathcal{D}_i^{\rho} \\ \dfrac{\mathrm{d}\boldsymbol{u}_i}{\mathrm{d}t} &= -\dfrac{\boldsymbol{\nabla} p_i}{\rho_i} + \dfrac{\mathbf{div}\left(\rho_i \boldsymbol{u}_i \otimes \delta\boldsymbol{u}_i\right)}{\rho_i} + \boldsymbol{F}_i^{v} + \boldsymbol{g} + a_{tank}(t)\,\boldsymbol{i} \\ \dfrac{\mathrm{d}\boldsymbol{r}_i}{\mathrm{d}t} &= \boldsymbol{u}_i + \delta\boldsymbol{u}_i, \quad V_i(t) = m_i \,/\rho_i(t), \quad p_i = c_0^2(\rho_i - \rho_0) \end{cases} \tag{3}$$

where m_i and $\boldsymbol{F}_i^v$ are the mass and the net viscous force related to the ith particle, while $\mathcal{D}_i^{\rho}$ is a numerical diffusive term for stabilising the numerical scheme avoiding spurious noise in the pressure field. For the sake of brevity $\mathcal{D}_i^{\rho}$ is not reported here, the interested reader can find more details in Antuono et al. (2012) and more specifically in Antuono et al. (2021a), Meringolo et al. (2019) where the intensity of this term is determined dynamically in space and time.

The spatial differential operators are approximated by:

$$\begin{cases} \mathrm{div}(\boldsymbol{u}_i) = \displaystyle\sum_j (\boldsymbol{u}_j - \boldsymbol{u}_i)\cdot\boldsymbol{\nabla}_i W_{ij} V_j \quad ; \quad \mathrm{div}(\delta\boldsymbol{u}_i) = \sum_j (\delta\boldsymbol{u}_j - \delta\boldsymbol{u}_i)\cdot\boldsymbol{\nabla}_i W_{ij} V_j \\ \mathrm{div}(\rho_i\delta\boldsymbol{u}_i) = \displaystyle\sum_j (\rho_i\delta\boldsymbol{u}_i + \rho_j\delta\boldsymbol{u}_j)\cdot\boldsymbol{\nabla}_i W_{ij} V_j \quad ; \quad \boldsymbol{\nabla} p_i = \sum_j (p_i + p_j)\boldsymbol{\nabla}_i W_{ij} V_j \\ \mathrm{div}(\rho_i\boldsymbol{u}_i \otimes \delta\boldsymbol{u}_i) = \displaystyle\sum_j (\rho_i\boldsymbol{u}_i \otimes \delta\boldsymbol{u}_i + \rho_j\boldsymbol{u}_j \otimes \delta\boldsymbol{u}_j)\boldsymbol{\nabla}_i W_{ij} V_j \,, \end{cases}$$

where the j index refers to neighbour particles of ith particle. The spatial gradients are approximated through the convolution with a kernel function W_{ij}. A C2-Wendland kernel is adopted in the present work (see Wendland, 1995).

Initially the particles are distributed on a Cartesian lattice with spacing Δx, consequently the volumes V_{i0} at time $t = 0$, are initialised as Δx^3. Regarding the radius of the support of the kernel W, this is fixed to $2h = 2.7\Delta x$, being h the smoothing length.

The particle masses m_i are calculated through the initial pressure field, *i.e* $m_i = \rho_{i0} V_{i0}$ and they remain constant during the time evolution; while the volumes V_i change in time accordingly with the particle density, *i.e.* $V_i(t) = m_i/\rho_i(t)$.

The viscous force acting on ith particle is computed through the formulation described in Monaghan (2005) and contains both the effect of the physical viscosity μ and the turbulent stresses μ_i^T (see also Lo and Shao, 2002; Rogers and Dalrymple, 2005):

$$\begin{cases} \boldsymbol{F}_i^{v} &:= \dfrac{10}{\rho_i}\displaystyle\sum_j (\mu + \mu_{ij}^T)\,\pi_{ij}\,\nabla_i W_{ij}\,V_j\,, \quad \pi_{ij} := \dfrac{(\boldsymbol{u}_i - \boldsymbol{u}_j)\cdot(\boldsymbol{r}_i - \boldsymbol{r}_j)}{\|\boldsymbol{r}_i - \boldsymbol{r}_j\|^2}\,, \\ \mu_{ij}^T &:= 2\,\dfrac{\mu_i^T\,\mu_j^T}{\mu_i^T + \mu_j^T}\,, \quad \mu_i^T := \rho_0\left[C_S(1-\exp^{-y_i^+/25})\,2h\right]^2 \|\mathbb{D}_i\| \end{cases} \tag{4}$$

where C_S is the Smagorinsky constant, set equal to 0.18 (see Smagorinsky, 1963; Bailly and Comte-Bellot, 2015), while $\|\mathbb{D}\|$ is a rescaled Frobenius norm, namely $\|\mathbb{D}\| = \sqrt{2\mathbb{D}:\mathbb{D}}$. In the present work the subgrid model for the turbulent viscosity is needed because of the high Reynolds number related to the simulations with water. More details related to the LES modelling rewritten in a quasi-Lagrangian formalism can be found in Di Mascio et al. (2017), Antuono et al. (2021a). In order to damp the turbulent eddy viscosity μ_T near the wall boundaries, a classical van Driest damping function is employed (see Van Driest, 1956) using:

$$y_i^+ = y_i\,\frac{u_{\tau i}}{\nu}\,, \quad u_{\tau i} = \sqrt{\frac{\tau_{wi}}{\rho_i}}\,, \quad \tau_{wi} = \mu\,\frac{\partial \boldsymbol{u}_i}{\partial \boldsymbol{n}_k}\bigg|_{wall}$$

where the normal gradient to the wall is evaluated considering the velocity $\boldsymbol{u}_i$ and the distance y_i of the ith particle from the wall and using $\boldsymbol{n}_k$ as the unitary vector to the wall associated to the kth node closest to the ith particle.

Finally, the scheme is integrated in time using a 4th-order Runge–Kutta scheme for which the time-step Δt is obtained by means of CFL conditions as in Michel et al. (2022):

$$\Delta t = \min\left(0.031 \min_i \frac{(2h)^2\,\rho_i}{(\mu + \mu_i^T)} \;\;,\;\; 0.3 \min_i \sqrt{\frac{\Delta x}{\|\boldsymbol{a}_i\|}} \;\;,\;\; 0.6\,\frac{2h}{c_0} \right)$$

where $\|\boldsymbol{a}_i\|$ is the particle acceleration. Even for the lowest Reynolds number considered in the present article, the last two constraints are always dominant with respect to the first one related to the viscous diffusion process.

2.3. Enforcement of the boundary conditions

The solution of the governing equations (1) requires the definition of the boundary conditions on the free surface and on the tank walls. As discussed in Colagrossi et al. (2009, 2011), the kinematic and dynamic conditions of the free surface are intrinsically satisfied in SPH methods.

The adherence boundary condition on the solid surface can be enforced through a ghost-fluid approach (see *e.g.* Macia et al., 2011; Antuono et al., 2023 and also Antuono et al., 2021b; Oger et al., 2016 where a quasi-Lagrangian formulation is used). The latter requires that at least five particles should be present within the boundary layer region. An estimation of the wall boundary thickness (WBT) can be obtained using the Blasius equation, and for the water test-case (Reynolds number is about 250,000) it results that the WBT is less than one millimetre and at the maximum spatial resolution only one SPH particle is present in the boundary layer region. For this reason the free-slip condition is enforced for the water test-case while for the other three liquids the no-slip condition can be applied. Similar hypothesis was also used in previous works (Marrone et al., 2021a; Michel et al., 2022; Malan et al., 2022).

2.4. Evaluation of the slosh dissipation

Following the analysis performed in Marrone et al. (2021b), Michel et al. (2022), the δ-LES-SPH energy balance can be written as:

$$\begin{cases} \dot{\mathcal{E}}_K + \dot{\mathcal{E}}_P - \mathcal{P}_{NF} = \mathcal{P}_V + \mathcal{P}_V^{turb} + \mathcal{P}_N \\ \mathcal{E}_K(t) = \dfrac{1}{2}\sum_i m_i\, u_i^2\,, \quad \mathcal{E}_P(t) = \sum_i m_i\, g\, z_i\,, \quad \mathcal{P}_{NF} = \sum_i m_i\, a_{tank}(t)\, \boldsymbol{i}\cdot\boldsymbol{u}_i \end{cases} \tag{5}$$

where on the left-hand side, $\mathcal{E}_K$ and $\mathcal{E}_P$ are the kinetic and potential energy of the particle system. For $\mathcal{E}_P$ the vertical position of the generic i-th particle is indicated with z_i. $\mathcal{P}_{NF}$ is the power linked to the non-inertial forces.

The elastic potential energy linked to the compressibility of the liquid is negligible within the weakly-compressible assumption; hence, it is not considered in the energy balance (for more details see Antuono et al., 2015).

The right-hand side of the energy balance (5) contains the dissipation terms due to the real viscosity $\mathcal{P}_V$, the turbulent viscosity $\mathcal{P}_V^{turb}$, to numerical diffusion $\mathcal{P}_N$. In the specific, the latter takes into account the effect of the density diffusion and the particle shifting $\delta\boldsymbol{u}$ (see Michel et al., 2023). The power related to the viscous forces is directly evaluated through the expression (4) as:

$$\mathcal{P}_V + \mathcal{P}_V^{turb} = 10 \sum_i \sum_j (\,\mu + \mu_{ij}^T\,)\,\pi_{ij}\,\boldsymbol{u}_i\cdot\nabla_i W_{ij}\, V_i\, V_j \tag{6}$$

where the quantity $\mathcal{P}_V^{turb}$ refers to the viscous dissipation of the modelled sub-grid scales, whereas $\mathcal{P}_V$ refers to the resolved scales. The energy dissipated by the fluid is then evaluated by integrating in time equation (5):

$$\begin{cases} [\mathcal{E}_K + \mathcal{E}_P](t) - [\mathcal{E}_K + \mathcal{E}_P](t_0) - \mathcal{W}_{NF}(t) = \mathcal{E}_{diss}(t)\,, \\ \mathcal{W}_{NF}(t) = \displaystyle\int_{t_0}^{t} \left[\sum_i m_i\,(-a_{tank}\,\boldsymbol{i}\cdot\boldsymbol{u}_i)\right] dt\,, \quad \mathcal{E}_{diss}(t) = \int_{t_0}^{t} \left(\mathcal{P}_V + \mathcal{P}_V^{turb} + \mathcal{P}_N\right) dt \end{cases} \tag{7}$$

where W_{NF} is the work performed by the non-inertial forces on the fluid and $[\mathcal{E}_K + \mathcal{E}_P](t_0)$ is the mechanical energy related to the time instant t_0.

The first equation of (7) provides two ways for the evaluation of the energy dissipated by the fluid: (i) the first is using the left-hand side of the first equation; (ii) a second way is to directly estimate $\mathcal{E}_{diss}$ using the second equation in which the three dissipation terms are integrated in time. Both these approaches were adopted in the present simulations in order to verify that the present model is able to close the energy balance accurately (see also *e.g.*, Malan et al., 2022; Marrone et al., 2023).

Considering that the fluid is at rest in the initial condition, the energy balance (7) can be reshaped as:

$$\begin{cases} \mathcal{E}_K(t) + m_l\, g\, \left[z_G(t) - z_G(t_0)\right] + m_l \displaystyle\int_{t_0}^{t} \dot{x}_G(\tau)\, a_{tank}(\tau)\, d\tau = \mathcal{E}_{diss}(t)\,, \\ x_G(t) := \dfrac{\sum_i m_i\, x_i(t)}{m_l}\,, \qquad z_G(t) := \dfrac{\sum_i m_i\, z_i(t)}{m_l}\,, \end{cases} \tag{8}$$

where x_G and z_G are the horizontal and vertical coordinates of the liquid centre of mass in the Ni-FoR, being $m_l = \sum_i m_i$ the total mass of the liquid inside the tank.

Following again Marrone et al. (2021b), one can find that the acceleration of the centre of mass $a_G(t) = \ddot{x}_G(t)$ along the x-axis, is linked to the horizontal forces F_x that the liquid exerts on the tank:

$$m_l\, a_G(t) = -F_x(t) - m_l\, a_{tank}(t) \tag{9}$$

and the work performed by those forces is:

$$\begin{aligned} \mathcal{W}_{ext}^{dyn}(t) &= m_l \int_{t_0}^{t} a_G(\tau)\, u_{tank}(\tau)\, d\tau = \\ &= -\int_{t_0}^{t} F_x(\tau)\, u_{tank}(\tau)\, d\tau - \frac{m_l}{2}\left[u_{tank}^2(t) - u_{tank}^2(t_0)\right] \end{aligned} \tag{10}$$

where u_{tank} is the velocity of the tank. If the fluid is "frozen" (*i.e.*, no liquid sloshing), the above external work performed by the tank walls on the fluid is zero since the horizontal position of the centre of mass x_G is a constant in the Ni-FoR and the work of the external force F_x is just linked to the change of the kinetic energy of the frozen liquid.

If we consider that the tank oscillates with an harmonic law, using integration by parts, it follows that:

$$\mathcal{W}_{ext}^{dyn}(t_0 + T) = m_l\, \left[\dot{x}_G(t)\, u_{tank}(t)\right]_{t_0}^{t_0+T} + \mathcal{W}_{NF}(t_0 + T) \tag{11}$$

where, as explained in Marrone et al. (2021b), the first term on the right-hand side is linked to differences in the mechanical energy evaluated in the Inertial frame of reference (I-FoR) and in the Ni-FoR. If the liquid sloshing reaches a "quasi periodic condition" this term is negligible and the two work terms W_{ext}^{dyn} and W_{NF} almost coincide and are practically both equal to the dissipated energy. Because of the highly non-linear behaviour of the sloshing phenomenon, in Section 3 it is shown that the quasi-periodicity of the fluid can be reached only after long time evolution (see also Marrone et al., 2023). Besides this, in all the test-cases studied in Section 3 the "quasi periodic" condition is reached in the final parts of the simulations.

In particular, in the quasi-periodic regime the energy dissipated during the kth period can be evaluated as:

$$\mathcal{E}_{diss}^{(k)} = -m_l \int_{kT}^{kT+T} a_G(\tau)\, u_{tank}(\tau)\, d\tau \tag{12}$$

As shown in Section 3.4, after the transitory stage lasting N_{P0} periods, $\mathcal{E}_{diss}^{(k)}$ remains almost constant for $k > N_{P0}$, hence, it is possible to associate an average dissipation power during N_p periods as:

$$\overline{\mathcal{P}}_{diss} = -\frac{m_l}{N_P\, T} \int_{N_{P0}\, T}^{(N_{P0}+N_P)\, T} a_G(\tau)\, u_{tank}(\tau)\, d\tau \tag{13}$$

The above equation highlights the role of the motion of the fluid centre of mass in the Ni-FoR concerning the energy dissipated by the liquid sloshing. The phase lag between the horizontal tank motion $x_{tank}(t)$ and the fluid centre of mass $x_G(t)$ plays a crucial role in the slosh dissipation (see *e.g.* Marrone et al., 2021b, Marrone et al., 2021a, Malan et al., 2022). As clear from Eq. (13), high dissipation is obtained when $a_G(t)$ and $u_{tank}(t)$ are in phase, while low dissipation occurs when they are in quadrature (see Section 3.3 and also Marrone et al., 2023; Saltari et al., 2022; Malan et al., 2022).

3. Numerical results

3.1. Description of the test-case

In the present work, the experimental test-case analysed in Faltinsen et al. (2005a) is considered. A square-base tank is adopted with length, width and height denoted with L, W and D whose values are reported in Fig. 1. The filling height is set equal to $H = 0.508\, L$. The tank is forced to oscillate in the horizontal x direction with a prescribed time law:

$$x_{tank}(t) = A(t)\, \sin\left(\frac{2\,\pi\, t}{T}\right)\,, \qquad A(t) = A\, \mathrm{erf}\left(\frac{2t}{\tau}\right) \tag{14}$$

where the maximum amplitude A is equal to $0.0156L$ and the ramp time $\tau = 15\,T$, which means that $A(t)$ practically reaches its maximum value A after 15 oscillation periods. The oscillation period T is set equal to the lowest natural one $T_1 = 0.9059$ s. The final time of the simulation is equal to $t_{fin} = 85\,T$.

Four different liquids are considered: water, sunflower oil, castor oil and glycerin. Table 1 reports the liquid mass m_l, the kinematic

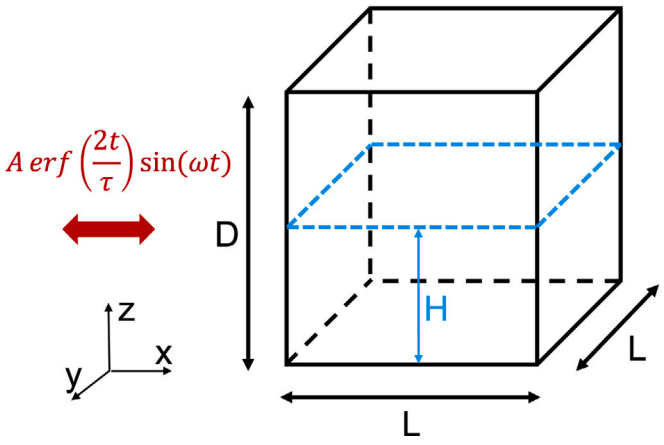

L [cm]	59
W [cm]	59
D [cm]	89
H [cm]	30
A [cm]	0.92
T [s]	0.9059

Fig. 1. Left: sketch of the tank. Right: geometric tank sizes of the experiments by Faltinsen et al. (2003) and amplitude A and period T of the harmonic motion imposed to the tank.

Table 1
Liquids adopted in the simulations: m_l is the total liquid mass, ν the kinematic viscosity, $\Delta\mathcal{E}$ the reference energy, $\Delta\mathcal{P}$ the reference power and Re the Reynolds number of the sloshing flow.

Test N°	Label	m_l (Kg)	ν (m/s^2)	$\Delta\mathcal{E}$ (J)	$\Delta\mathcal{P}$ (W)	Re $=\frac{\sqrt{gH}\,H}{\nu}$
1	Water	104.1	$1.02\,10^{-6}$	153.1	1.988	253,100
2	Sunflower Oil	131.7	$4.99\,10^{-5}$	138.9	1.804	5155
3	Castor Oil	93.9	$1.04\,10^{-4}$	147.4	1.914	2469
4	Glycerin	100.3	$1.20\,10^{-3}$	193.6	2.514	214.8

viscosity ν (at temperature 25 °C), the reference energy $\Delta\mathcal{E} = 1/2\, m_l\, g\, H$ (which is the initial potential energy with respect to the tank bottom), the reference power $\Delta\mathcal{P} = \Delta\mathcal{E}/(nT)$ ($n = 85$ is the number of periods simulated) and the Reynolds number (defined as Re $= \sqrt{gH}\,H/\nu$) related to the different liquids.

3.2. Flow regimes and features

In this section the different sloshing regimes developed during the 85 oscillation periods are discussed for the four different liquids. The numerical simulations were performed with a spatial resolution $H/\Delta x = 80$ (*i.e.* the initial filling height H is discretised with 80 particles). It follows that the fluid domain is discretised with a total number of particles of $157 \times 157 \times 80 \approx 2$ millions. All the simulations were also executed with two coarser spatial resolutions $H/\Delta x = 60$ and $H/\Delta x = 40$ to check the influence of the number of particles on the obtained results as well as to measure the rate of convergence of the slosh dissipated energy (see Section 3.4).

In order to identify the different flow regimes, the time histories of the mechanical energy $\mathcal{E}_M$ of the fluids (*i.e.* sum of kinetic and potential energy) is analysed. Fig. 2 sketches the time histories of $\mathcal{E}_M$ for the four liquids. The top plot refers to the water test-case. It is possible to see that $\mathcal{E}_M$ exhibits a complex behaviour in time. We first identify the first regime I, where the mechanical energy increases up to a maximum value. This time is close to the end of the time ramp of the tank motion (see Eq. (14)). Within this first regime the tank walls act a positive work which is directly converted in an increase of the liquid motion inside the tank (see Section 2.4), *i.e.*:

$$\mathcal{W}_{ext}^{dyn}(t_I) = \int_{t_0}^{t_I} -F_x(t)\,u_{tank}(t)\,dt > 0$$

where $[t_0, t_I]$ is the time range of the regime I. Increasing the liquid viscosity, the maximum of $\mathcal{E}_M$ reached in the regime I decreases because of the reduction of the liquid motion. The first row of Fig. 3 shows the free surface configuration at the end of the regime I for the four different liquids.

The second regime II is quite counter-intuitive since the mechanical energy largely decreases. For the water test-case it reaches a minimum value close to zero which means that the liquid motion inside the tank almost stops (see second row of Fig. 3). In this regime the liquid returns the energy accumulated during the stage I to the tank walls, that is, the tank walls act a negative work on the fluid *i.e.*:

$$\mathcal{W}_{ext}^{dyn}(t_{II}) - \mathcal{W}_{ext}^{dyn}(t_I) = \int_{t_I}^{t_{II}} -F_x(t)\,u_{tank}(t)\,dt < 0$$

During the regime III the mechanical energy of the fluid increases again for all the fluids except for the glycerin where $\mathcal{E}_M$ oscillates around a constant value. For the water test-case the sloshing motion becomes more violent than the regime I, as displayed in the last two rows of Fig. 3. A transverse symmetric wave system (y direction) is generated whose wave length is half of the tank size. The amplitude of this transverse wave system increases in time and, eventually, the jet run-up on the tank edges collapses giving rise to the first breaking event in correspondence of the edge middle point (see Fig. 3 at time $t = 20.5T$). This behaviour is also documented experimentally in Faltinsen et al. (2003).

Finally, the regime IV is the last one recorded where the swirling wave instability takes place. This regime does not appear only in the glycerin test-case where the high viscous level inhibits this instability (see Fig. 4). In the water test-case the swirling mode is characterised by a violent motion of the free surface with the occurrence of roof impacts and several breaking events. The latter are also observed for the sunflower oil test-case but in smaller number and considerably less energetic. Conversely, for the castor oil test case the swirling occurs without any breaking events. In the water and the castor oil test-cases clockwise swirling waves take place, while for the sunflower oil anticlockwise motion occurs (see also Section 3.3). As also commented in Chen et al. (2023) the direction of rotation depends on the ramp $A(t)$ (see Eq. (14)) and, numerically, can also depend on parameters such as the spatial resolution $N = H/\Delta x$.

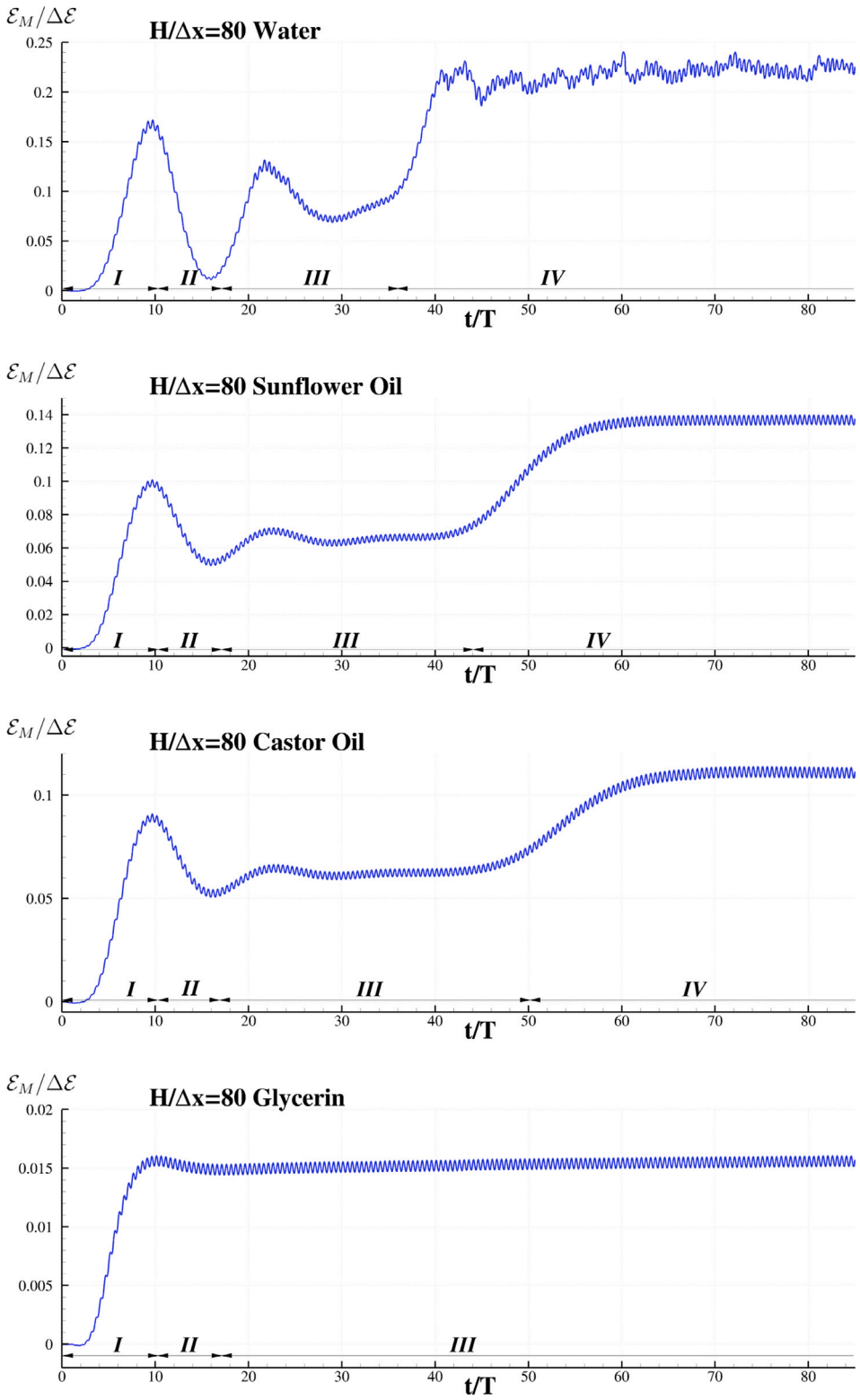

Fig. 2. Time histories of the mechanical energy for the four different liquids at the maximum spatial resolution $H/\Delta x = 80$.

3.3. Forces and tank motion

A further comparison is performed on the horizontal force components to describe the different behaviour of the four fluids. The different regimes previously described in Section 3.2 are also distinguishable in Fig. 5, in particular for the water test-case. Non-dimensional forces are computed using the liquid weight $F_{ref} = m_l\, g$.

Differently from the F_x component, which is related to the tank motion and the work exchanged between liquid and the walls, the F_y component is strictly connected with the onset of the swirling instability caused by the transition from planar wave (2D wave oscillating in x direction) to rotational ones. Looking at F_y evolution, the instability firstly starts in the water test-case, followed by sunflower and castor oil. In the glycerin case the swirling instability does not appear at all,

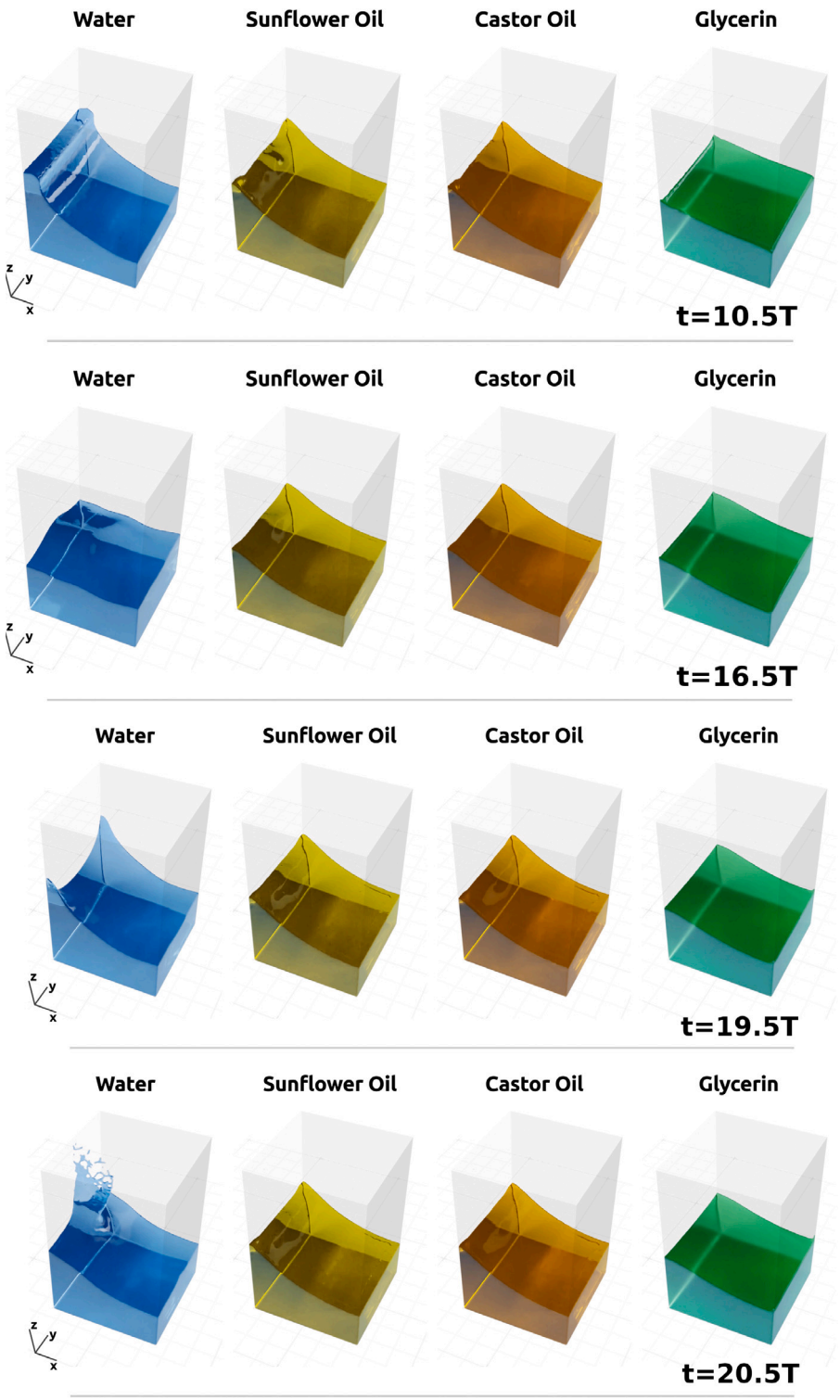

Fig. 3. Free-surface configurations for time instants $10.5T$, $16.5T$, $19.5T$ and $20.5T$ for the four different liquids. The full video of the simulation is available at Link Video N1.

remaining in a plane wave sloshing regime. This was further checked by extending that simulation up to 150 periods. It is worth remarking that, for all the swirling cases, the force F_x increases in amplitude after the development of swirling instability.

Fig. 6 depicts the amplitude of the Fourier transform of the horizontal force component F_x for the four liquids evaluated when the final stable regime is reached. In the abscissa the frequency are made dimensionless using the oscillation period, *i.e* $f^* = f\,T$. For the water test-case the spectrum is quite noisy and present three dominant peaks, related to the frequencies $f^* = 1, 3, 5$. The noisy behaviour is linked to the chaotic nature of the flow, where breaking phenomena and water impacts introduce erratic events in the time series. However, as shown in Fig. 7 the time series of F_x presents a time behaviour mainly dominated by the first and the third harmonics. In particular the third harmonic induces the presence of a double peak which is also observed in the experiments by Faltinsen et al. (2005a) and further commented

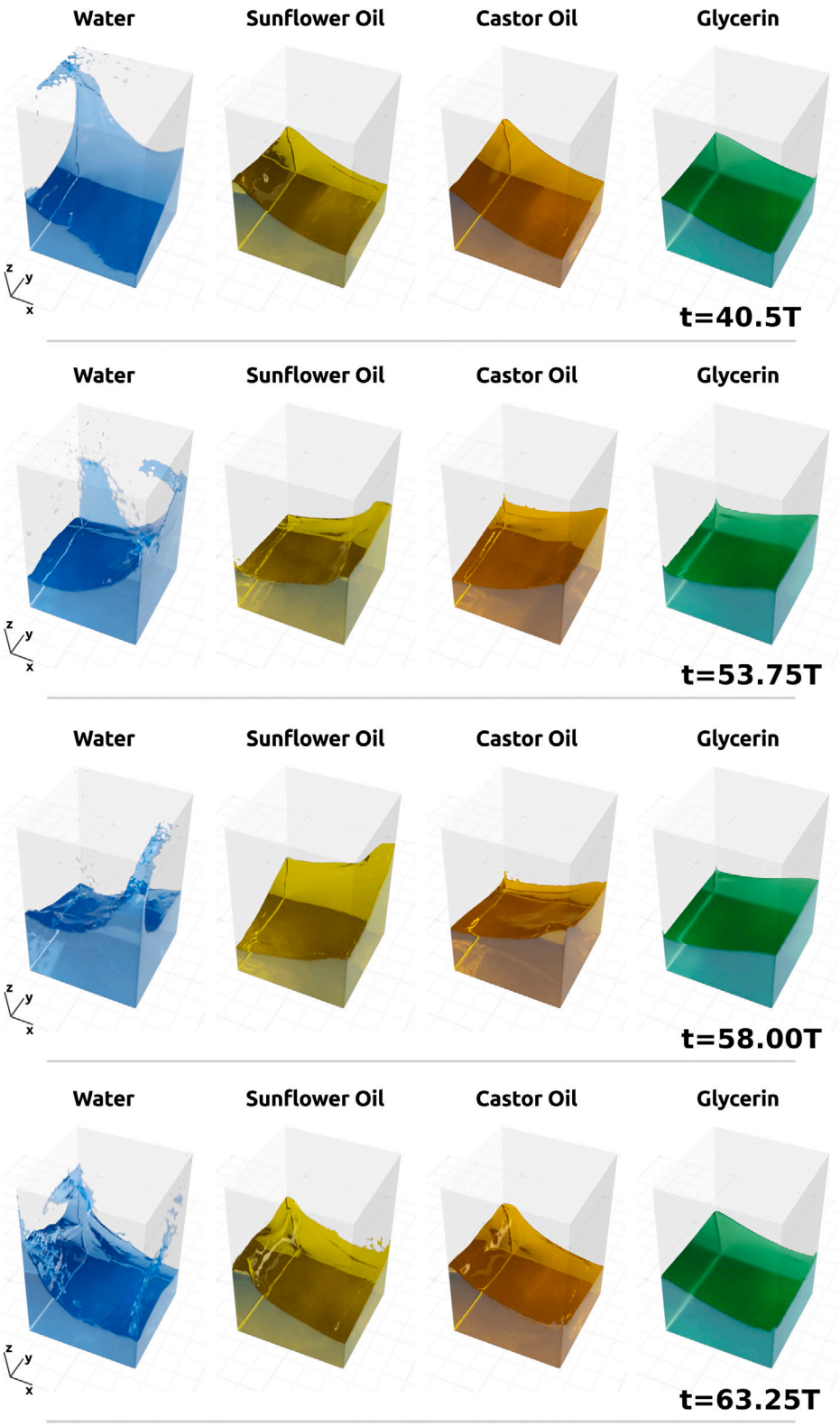

Fig. 4. Free-surface configurations for time instants $40.5T$, $53.75T$, $58T$ and $63.25T$ for the four different liquids. The full video of the simulation is available at Link Video N1.

in Appendix. Increasing the viscosity the frequency peaks $f^{=} * 1, 3, 5, 7$ and 9 appear more and more distinct and, at the same time, the weight of the 3rd harmonic becomes less relevant with respect to the intensity of the 1st harmonic. This behaviour is expected since in sloshing flows non-linear interactions generally become more significant with high Reynolds number.

The orbital evolution of the horizontal force components for the four fluids is reported in Fig. 8 as a function of time. Again for water, sunflower and castor oil the development of the swirling instability is evident. As for the water case, the high intensity of the free surface fragmentation, the frequent occurrence of roof impacts and several breaking events appear as a chaotic path of the orbit evolution in the

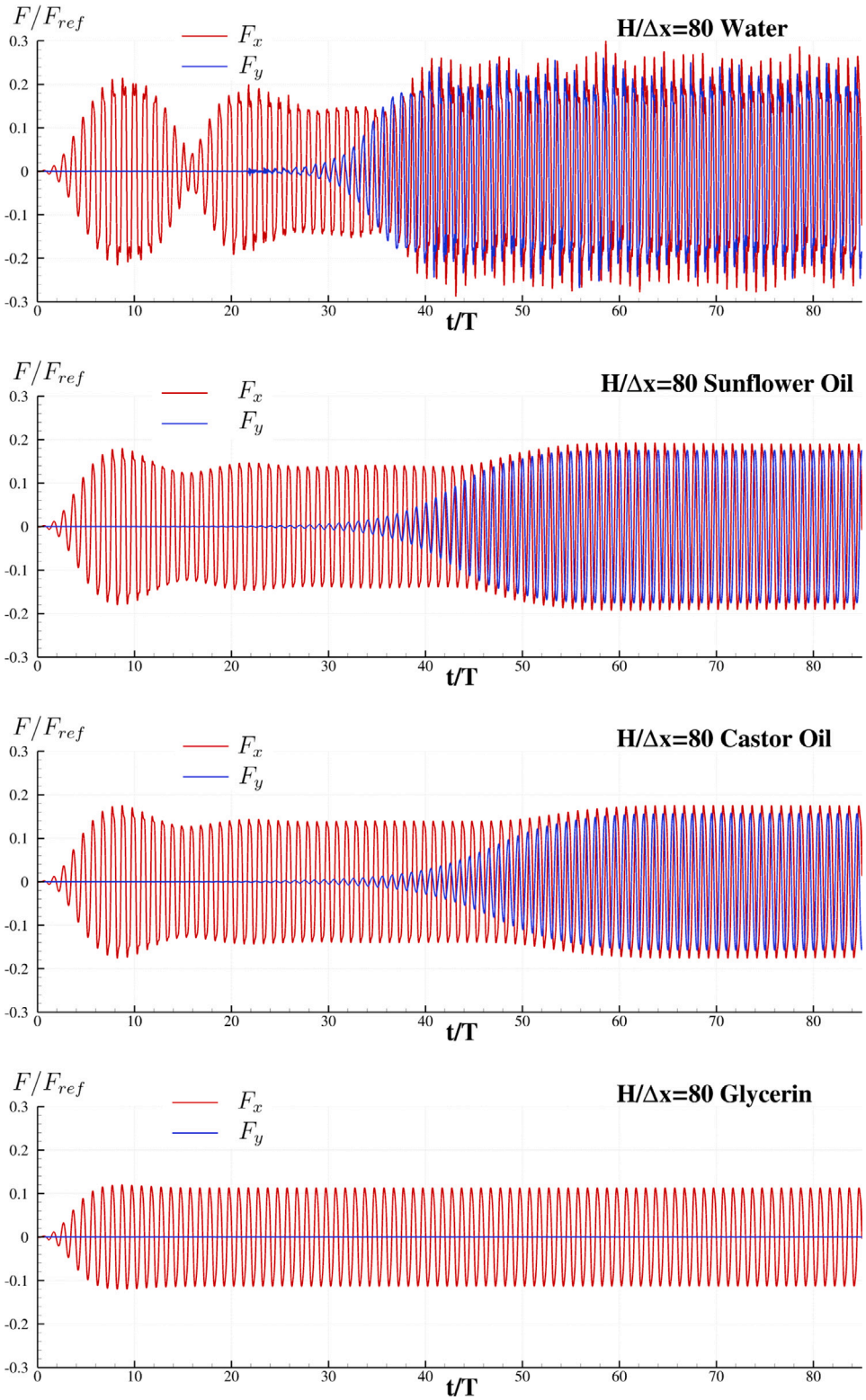

Fig. 5. Time history of horizontal force components, F_x and F_y, for the four different liquids. Non-dimensional forces are computed using the liquid weight $F_{ref} = m_l\, g$.

quasi-periodic flow regime. Conversely, in the oil cases, the orbits are much smoother and strictly follow a periodic path. On the contrary, glycerin oscillates periodically only in the x direction during the entire simulation.

The time evolution of the forces in the quasi-periodic regime creates orbits that can be inscribed in a parallelogram. The height of this parallelogram provides an indication about the intensity of the instability. In addition, the distance between the initial orbitals (coloured in yellow and red in Fig. 8) is linked to the celerity with which the swirling instability takes place.

A further comment can be made on the inclination of the parallelogram. The direction of the inclination gives information about the fluid rotation direction: water and castor oil cases feature a clockwise rotation whereas the sunflower oil anti-clockwise one. This is better

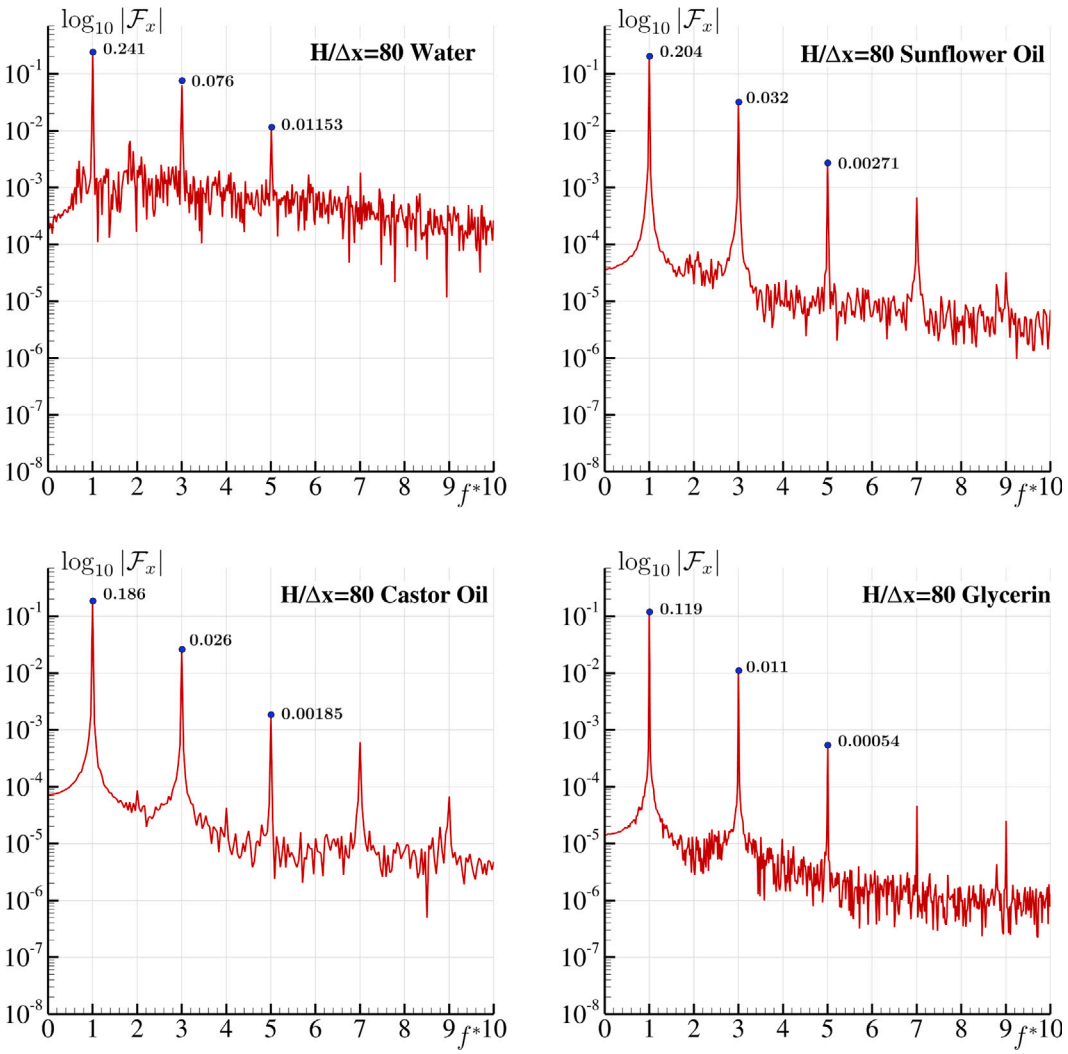

Fig. 6. Amplitude of the Fourier transform of the dimensionless horizontal force component F_x/F_{ref} for the four different liquids.

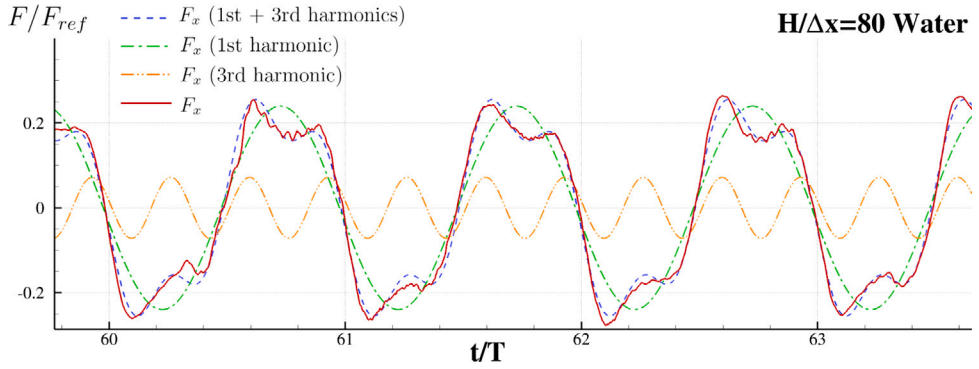

Fig. 7. Water test-case: reconstruction of the dimensionless horizontal force component F_x/F_{ref} using the first and third harmonics of the Fourier transform.

highlighted by Fig. 9 where the time evolution of torque M_z of the four liquids is reported. The average value in the quasi-periodic regime confirms the direction of swirling rotation: negative for clockwise rotation of water and castor oil, positive for anticlockwise direction of sunflower oil. Obviously, M_z is different from zero only when the swirling instability is established.

Finally, in Fig. 10 the time histories of the sloshing force $m_l\, a_G$ and of the imposed tank velocity are reported. As mentioned above, the time histories of the sloshing forces exhibit a clear periodic behaviour except for the water test-case for which a quasi-periodic regime is observed. As commented in Section 2.4 in periodic and quasi-periodic regimes the phase shift between the acceleration of the centre of mass $a_G(t)$ along the x-axis and the tank velocity $u_{tank}(t)$ is directly linked with the slosh dissipation. In particular, the maximum dissipation is attained when a_G and u_{tank} are in phase while the minimum dissipation occur when the two signals are in quadrature.

From Fig. 10 it is evident that phase shift is minimum for the water test-case while it is maximum for the glycerin one. Furthermore, the

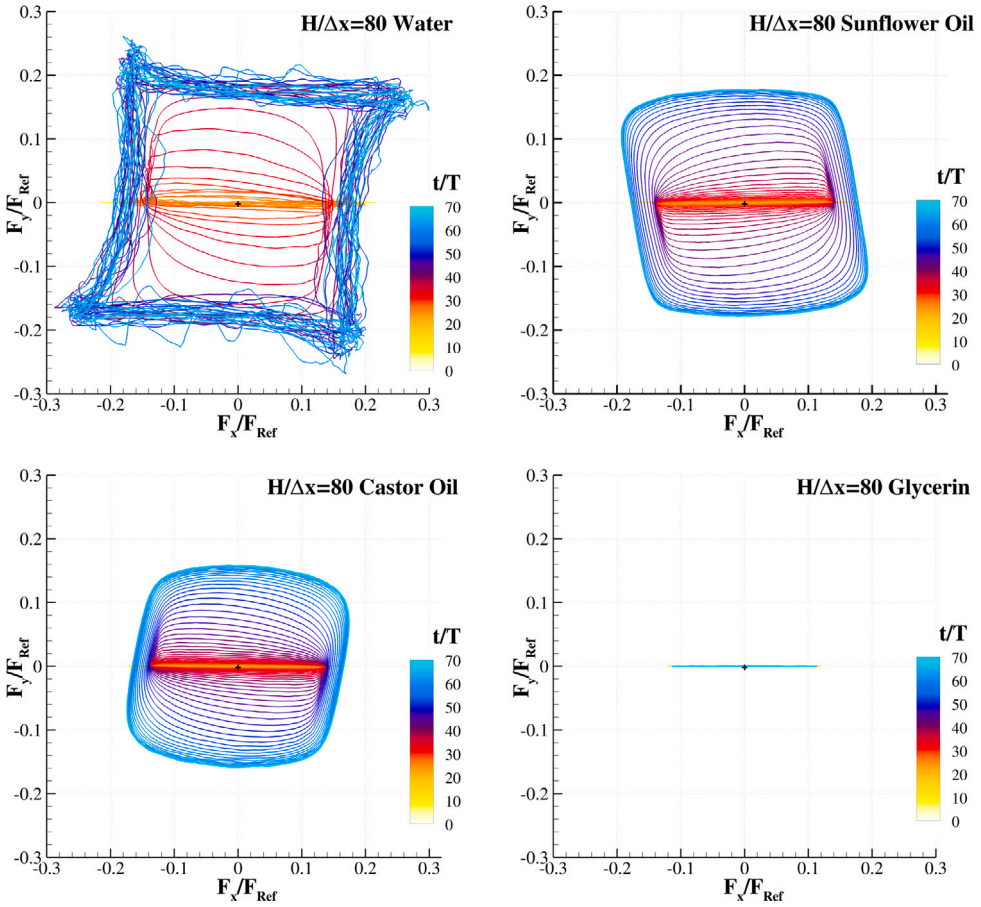

Fig. 8. Orbital evolution of the horizontal force components for the four liquids.

peak intensity is larger for water and decreases with the Reynolds number. As a consequence, for the water test-case a larger slosh dissipation is expected and it reduces as the viscosity increases, as further discussed in the next sub-section.

3.4. Energy dissipation

In the present section the time evolution of the main energy components is discussed. As introduced in Section 2.4 the energy balance is given by three primary terms:

$$\mathcal{E}_M - \mathcal{W}_{NF} = \mathcal{E}_{diss}$$

where $\mathcal{E}_M$ is the mechanical energy of the fluid in the Non-inertial frame of reference (Ni-FoR), $\mathcal{W}_{NF}$ is the work performed by the non-inertial forces and $\mathcal{E}_{diss}$ is the energy dissipated by the fluid. Fig. 11 shows the time behaviour of the three energy components for the four liquids. As for the water test-case, a change of steepness of E_{diss} is well visible when entering in the regime III and IV discussed in Section 3.2. Regime III is characterised by breaking waves and wall impact events which increase the dissipation rate. However, when the regime IV commences, corresponding to the establishment of the swirling motion, the dissipation rate reaches its maximum. The slope of $\mathcal{E}_{diss}$ remains almost constant in time being the flow in quasi-periodic regime. The double steepness behaviour of E_{diss} linked to the regime III and IV is evident also for the sunflower and castor oils.

A different behaviour characterises the glycerin test-case, for which E_{diss} exhibits a constant steepness just after a few oscillation periods. For this case the dissipation mechanism is mainly linked to the viscous forces in the boundary layer regions as the free-surface motion is smooth and periodic for the entire simulation.

As underlined in Colagrossi et al. (2015), the dissipation linked to the Viscous Boundary Layer (VBL) and the violent free-surface motion are two completely different mechanisms: in the water test-case the former is negligible; conversely, in the glycerin test-case the dissipation is essentially driven by the VBL. For the sunflower and castor oils the two mechanisms are coupled in a complex and non-linear way.

Table 2 reports the average dissipation rate $\overline{\mathcal{P}}_{diss}$ for the four liquids and for three different spatial resolutions. The upper part of the table contains the dimensionless number using the reference power $\Delta\mathcal{P}$ (see Table 1) whereas in the lower part the table reports the dimensional number in Watt. For both the cases the tendency is clear: the water test-case always presents the higher $\overline{\mathcal{P}}_{diss}/\Delta\mathcal{P}$ and $\overline{\mathcal{P}}_{diss}$ for all the simulations. Clearly, the liquids characterised by lower viscosity feature the highest flow dissipation rate thanks to the large motion of the free-surface and the several impact events. In the last row of Table 2 the order of convergence p is also reported. For all the test-cases a rate of convergence above the fist order is observed. As expected, for the glycerin test-case the highest p is obtained.

The dissipation rates of Table 2 are also reported in Fig. 12 against their associated Reynolds numbers in logarithmic scale. Even if the considered Reynolds numbers are few, it is evident that in both the graphs the rate of dissipation seems to have a complex dependency on log(Re). This is mainly linked to the combination of the two dissipation mechanisms: (i) the one related with the free-surface motion/fragmentation and (ii) the one linked to the VBL. This topic deserves further investigations with a more regular sampling of the considered Reynolds range and simulations with higher spatial resolutions for the largest Re numbers.

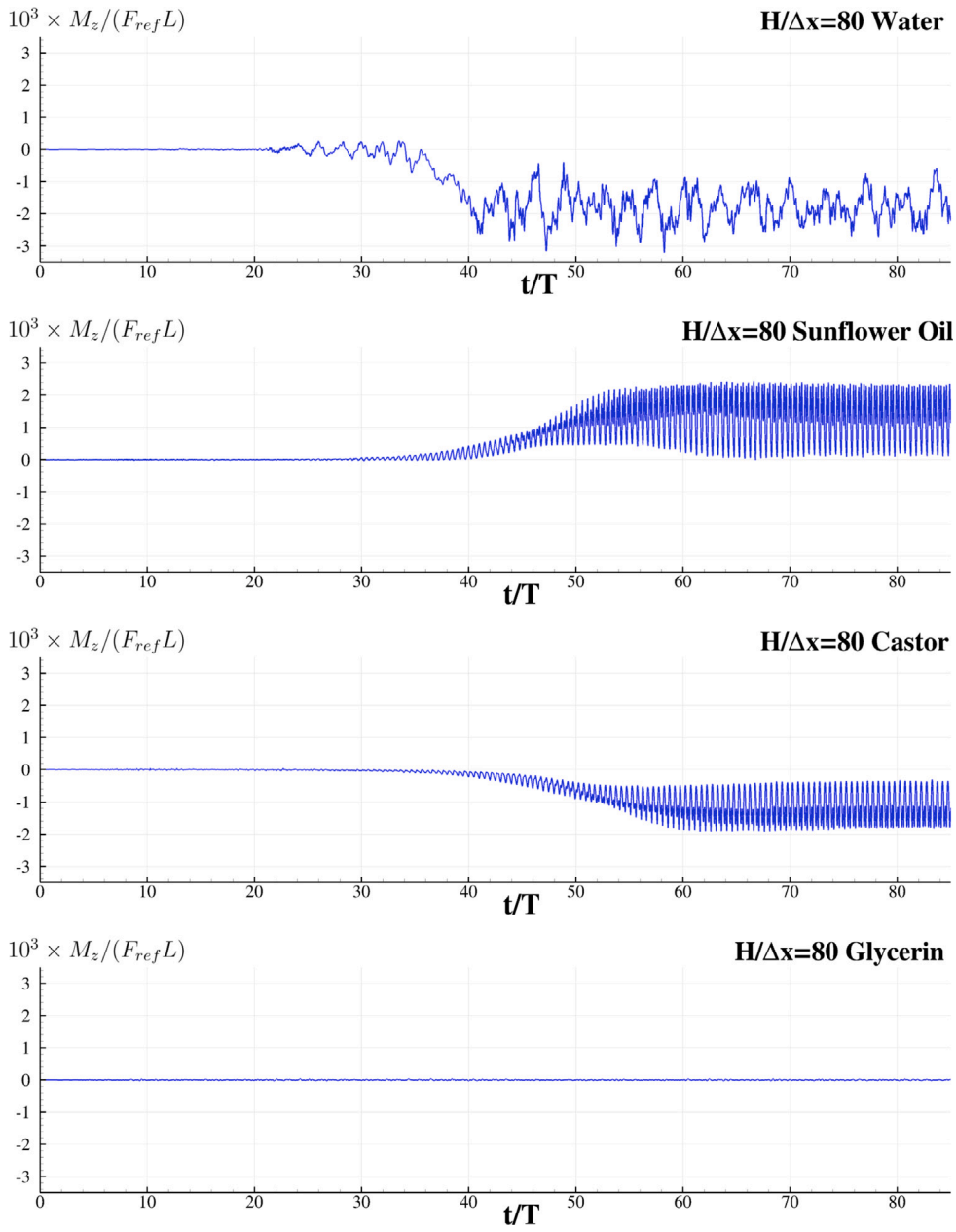

Fig. 9. Time evolution of the torque M_z for the four liquids.

Table 2
Rate of dissipated energy $\overline{\mathcal{P}}_{diss}$ in the quasi-periodic regime for the four liquids at different spatial resolution $N = H/\Delta x$. Dimensionless and dimensional values are reported, the latter are expressed in Watt. Symbol p indicates the measured convergence rate.

$\overline{\mathcal{P}}_{diss}/\Delta\mathcal{P}$	Water	Sunflower Oil	Castor Oil	Glycerin
$N = 40$	3.99	3.12	2.85	1.94
$N = 60$	3.87	3.22	2.84	1.89
$N = 80$	3.82	3.26	2.84	1.89
$\overline{\mathcal{P}}_{diss}$ (W)	Water	Sunflower Oil	Castor Oil	Glycerin
$N = 40$	7.93	5.63	5.46	4.86
$N = 60$	7.70	5.81	5.44	4.78
$N = 80$	7.59	5.89	5.43	4.75
p	1.12	1.33	1.02	1.81

3.5. CPU costs

Regarding the CPU costs, the SPH code adopted is an in-house research code (not optimised for industrial applications) with MPI parallelisation. For the water test-cases simulation, with $N = 80$ (about 2,000,000 particles), the SPH solver requires about 4 days on 192 cores for 260,000 time iterations ($\Delta t \simeq 0.3$ ms). For the lowest resolutions N=40 and N=60, 48 and 96 cores were used which ran, respectively, for 8 and 30 h. To run all the 12 simulations, *i.e.* four liquids with three different spatial resolutions, approximately 65,000 core hours were necessary.

The SPH simulations ran on the "Liger" supercomputer at Ecole Centrale de Nantes, which is equipped with 12-core Intel Xeon (Haswell) E5–2680v3 processors. We evaluated a computational speed defined as:

$$\eta = \frac{CPU_{time}\, N_{cores}}{N_{iteration}\, N_{particles}}, \tag{15}$$

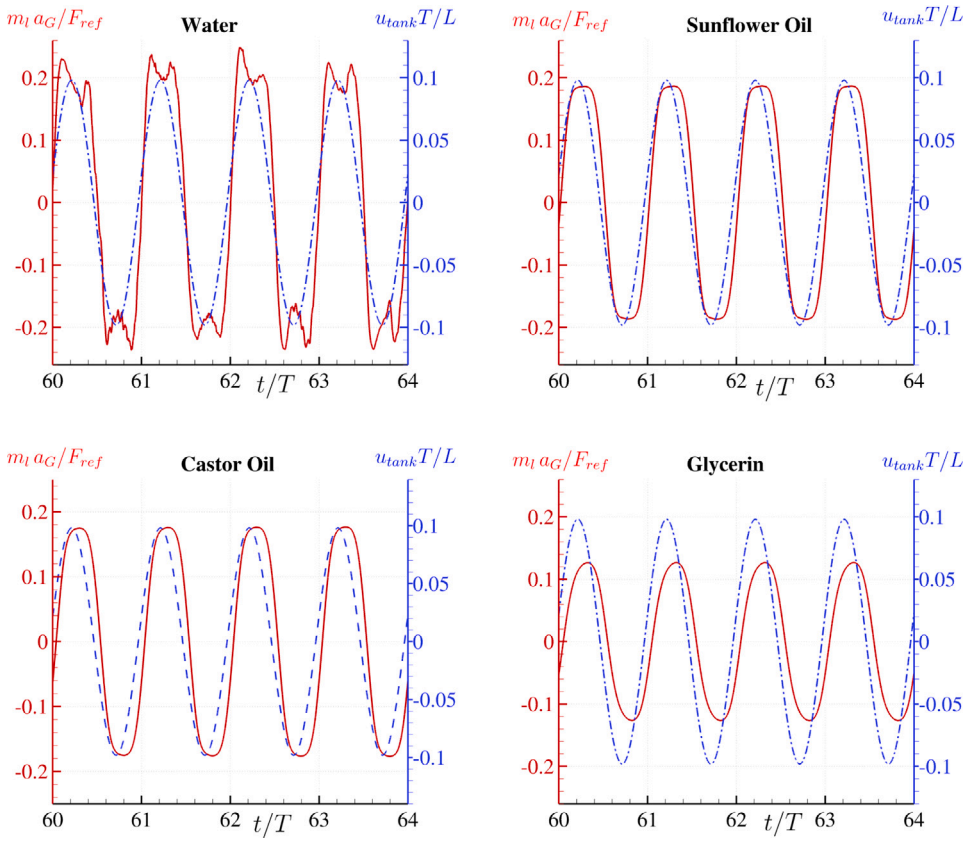

Fig. 10. Phase comparison of the sloshing force (red solid line) and tank motion (blue dash-dotted line) in the quasi-periodic regime.

and for our SPH solver $\eta = 120\,\mu s$. The performance of the present SPH solver are not far from other academic fluid dynamic solvers (see *e.g.* Malan et al., 2022). Moreover, the CPU costs are also related to the evaluation of the different energy components needed for the analysis presented in this work.

4. Conclusions

Swirling waves instability is numerically investigated using an enhanced version of the Smoothed Particle Hydrodynamic (SPH) model called δ-LES-SPH model. The flow is studied inside a 3D square-base tank with filling ratio of 50.8% forced with a horizontal motion at a frequency equal to the resonant one. The focus is on how viscosity influences this instability, considering four different liquids: water, sunflower oil, castor oil and glycerine. The resulting Reynolds numbers span from 200 up to 250,000.

Because of the highly non-linear behaviour of the sloshing phenomenon we showed that the swirling instability, when it is not inhibited by the viscosity, can be reached only after a long time transient stage. Thanks to the conservation properties of the SPH models, these simulations are obtained without accumulating significant errors on the main conservation quantities.

The different flows are studied by analysing the free-surface evolution as well as global quantities such as mechanical energy and forces exerted by the fluid. The latter are studied in detail also by means of Fourier transform and allowed to highlight the signatures of the different flows.

The results show that energy dissipation largely increases when the swirling instability takes place. The dissipation phenomenon is strictly linked to the free-surface fragmentation, occurring at higher Reynolds numbers. This is the case of water that exhibits a faster and more pronounced swirling instability and dissipates more energy during its rotating motion than the other three liquids characterised by higher viscosity. These observations confirm the conclusions drawn in other sloshing studies such as Bouscasse et al. (2014a), Calderon-Sanchez et al. (2023) where it is found that the damping sloshing flows is higher when less viscous liquid are used.

It is evident from the present work that the dependency of the dissipation rate on the fluid viscosity is complex across the considered range of Reynolds numbers. However, as only four test-cases were analysed, this topic deserves future investigations to describe more in details such a relation.

CRediT authorship contribution statement

C. Pilloton: Writing and the designing of the article, Simulations. **J. Michel:** Writing and the designing of the article, Simulations. **A. Colagrossi:** Writing and the designing of the article, Simulations. **S. Marrone:** Writing and the designing of the article, Simulations.

Declaration of competing interest

The authors declare that they have no known competing financial interests or personal relationships that could have appeared to influence the work reported in this paper.

Data availability

Data will be made available on request.

Acknowledgements

The work was supported by the “Siemens Digital Industries Software Chair” and simulation were performed by using HPC resources of the Centrale Nantes Supercomputing Centre on the cluster Liger.

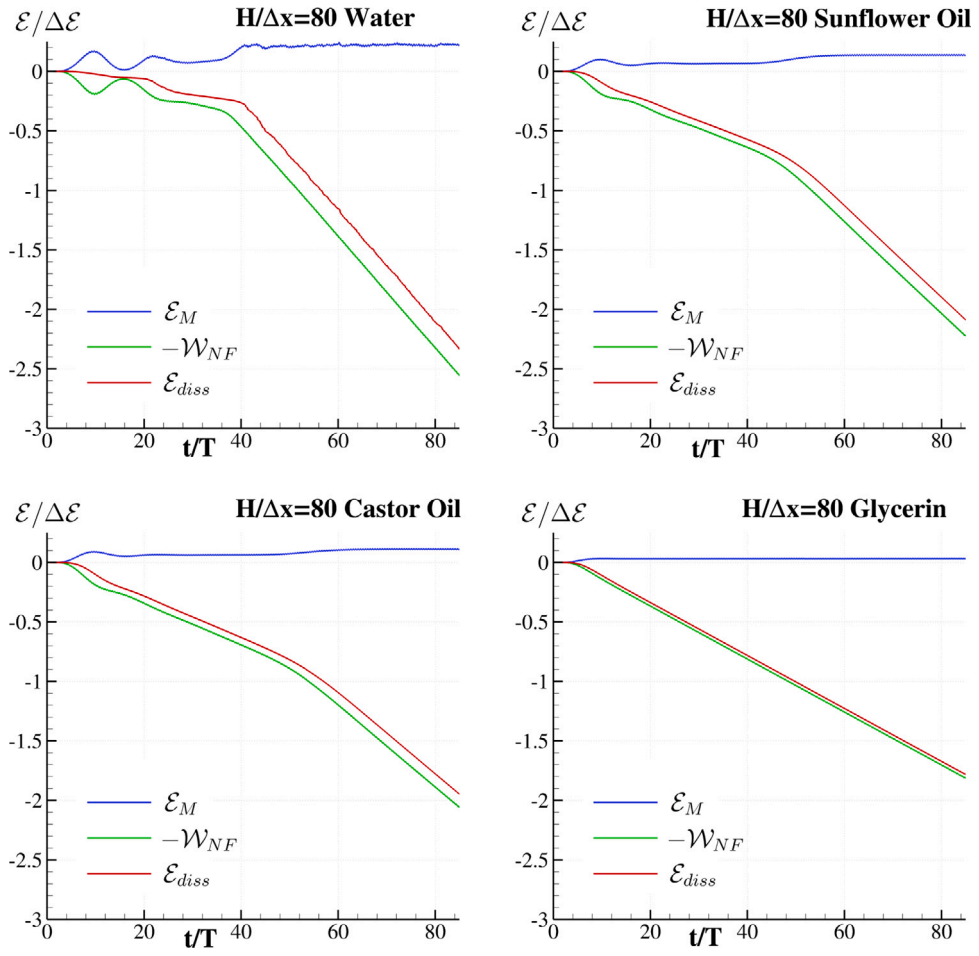

Fig. 11. Time evolution of the fluid mechanical energy $\mathcal{E}_M$ (evaluated in the Non-inertial frame of reference), the work $\mathcal{W}_{NF}$ performed by the non-inertial forces and the energy dissipated by the fluid $\mathcal{E}_{diss}$ for the four different test-cases.

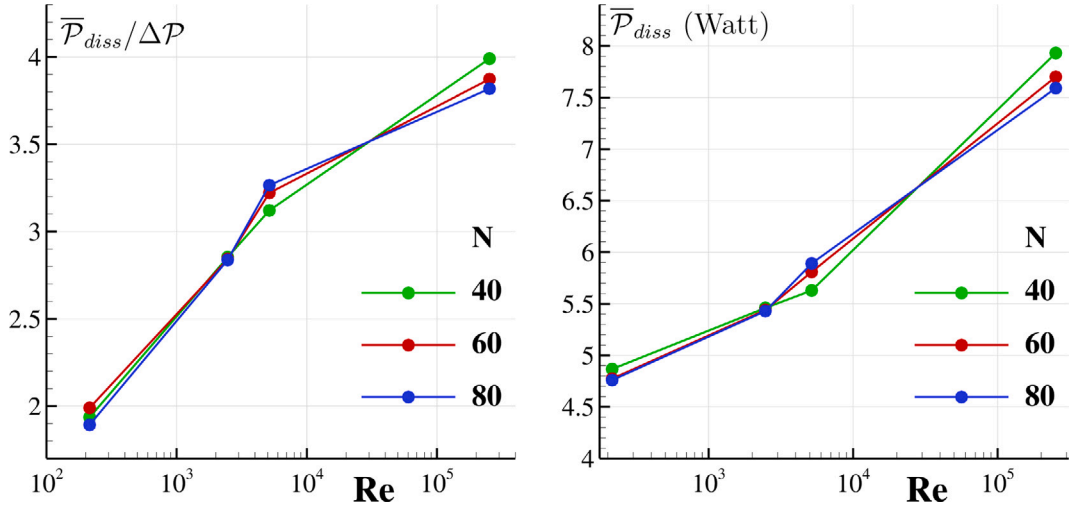

Fig. 12. Rate of dissipated energy $\overline{\mathcal{P}}_{diss}$ in the quasi-periodic regime for the four liquids at different spatial resolution $N = H/\Delta x$. Left: dimensionless values. Right: dimensional values in Watt.

The authors are most grateful to Paolo Colagrossi, CEO of Punkt.ink company, for the post-processing and the rendering of 3D SPH data.

The work was also partially supported by the SLOWD project which received funding from the European Union's Horizon 2020 research and innovation programme under grant agreement No 815044, and partially supported by the Italian "Ministero dell'Ambiente e Sicurezza Energetica" under the Grant Agreement "RdS PTR 2022–2024 - Energia elettrica dal mare".

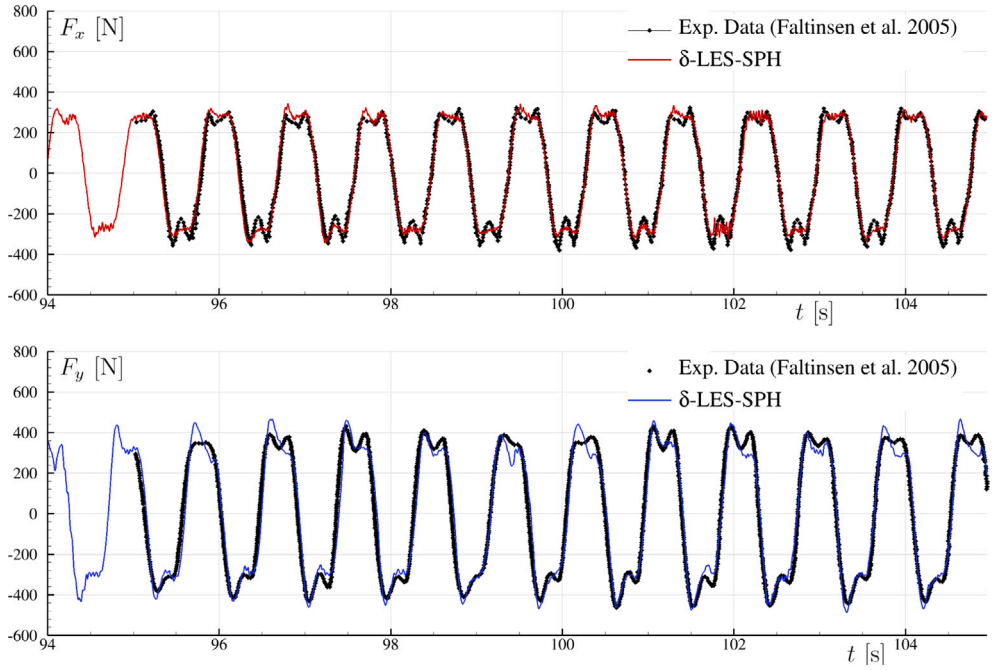

Fig. A.1. Comparison of the horizontal force components F_x and F_y as a function of time F_x (top) F_y (bottom): numerical results (solid line) and experimental results (dotted line) of Faltinsen et al. (2005a) with $H = 0.508\,L$, $T_1/T = 1.011$, $A = 0.46$ cm.

Appendix. Validation of the numerical method against experimental data

The δ-LES-SPH model adopted in present work has been widely validated in previous work (see *e.g.* Meringolo et al., 2019; Antuono et al., 2021a; Calderon-Sanchez et al., 2021; Malan et al., 2022; Marrone et al., 2021a; Michel et al., 2022; Marrone et al., 2023). A further validation is here performed simulating one of the swirling sloshing test-case proposed in Faltinsen et al. (2005a) for which experimental data on the forces are available. The test-case selected is the one with the filling height $H = 0.508L$, the tank forced longitudinally with an oscillation period that is $T_1/T = 1.011$ with an amplitude equal to $A = 0.46$ cm. The experiments was carried out with water and the numerical simulation is performed with a maximum spatial resolution $H/\Delta x = 80$.

Fig. A.1 depicts the comparison of the time histories of the horizontal force components F_x and F_y, in the steady state regime. Also for this test-case the swirling mode is excited and the time history of the F_x components shows a similar behaviour with double peaks already discussed in Section 3.3. As also remarked in Faltinsen et al. (2005a) this time behaviour is linked to the third and fifth harmonics. The δ-LES-SPH prediction of F_x is in a good agreement with the experimental data. Regarding the F_y component the experimental data show variations from one cycles to the other which is linked to the chaotic nature of the flow. For this reason local disagreements between experiments and numerical results are more visible.

References

Antuono, M., Colagrossi, A., Marrone, S., 2012. Numerical diffusive terms in weakly-compressible SPH schemes. Comput. Phys. Comm. 183, 2570–2580.

Antuono, M., Marrone, S., Colagrossi, A., Bouscasse, B., 2015. Energy balance in the δ-SPH scheme. Comput. Methods Appl. Mech. Engrg. 289, 209–226.

Antuono, M., Marrone, S., Di Mascio, A., Colagrossi, A., 2021a. Smoothed particle hydrodynamics method from a large eddy simulation perspective. Generalization to a quasi-lagrangian model. Phys. Fluids 33, 015102.

Antuono, M., Pilloton, C., Colagrossi, A., Durante, D., 2023. Clone particles: A simplified technique to enforce solid boundary conditions in SPH. Comput. Methods Appl. Mech. Engrg. 409, 115973.

Antuono, M., Sun, P., Marrone, S., Colagrossi, A., 2021b. The δ-ALE-SPH model: An arbitrary lagrangian-eulerian framework for the δ-SPH model with particle shifting technique. Comput. & Fluids 216, 104806.

Bailly, C., Comte-Bellot, G., 2015. The Dynamics of Isotropic Turbulence. Springer International Publishing, pp. 179–210.

Bongarzone, A., Marcotte, A., Gallaire, F., 2022. Super-Harmonically Resonant Swirling Waves in Longitudinally Forced Circular Cylinders. Bulletin of the American Physical Society.

Bouscasse, B., Colagrossi, A., Souto-Iglesias, A., Cercos-Pita, J., 2014a. Mechanical energy dissipation induced by sloshing and wave breaking in a fully coupled angular motion system. I. theoretical formulation and numerical investigation. Phys. Fluids 26, 033103.

Bouscasse, B., Colagrossi, A., Souto-Iglesias, A., Cercos-Pita, J., 2014b. Mechanical energy dissipation induced by sloshing and wave breaking in a fully coupled angular motion system. II. experimental investigation. Phys. Fluids 26, 033104.

Calderon-Sanchez, J., Martinez-Carrascal, J., González-Gutiérrez, L.M., 2023. Computational scaling of SPH simulations for violent sloshing problems in aircraft fuel tanks. Acta Mech. Sinica 39, 722051.

Calderon-Sanchez, J., Martinez-Carrascal, J., González-Gutiérrez, L., Colagrossi, A., 2021. A global analysis of a coupled violent vertical sloshing problem using an SPH methodology. Eng. Appl. Comput. Fluid Mech. 15, 865–888.

Chen, B.F., Wu, C.H., 2011. Effects of excitation angle and coupled heave–surge–sway motion on fluid sloshing in a three-dimensional tank. J. Mar. Sci. Technol. 16, 22–50.

Chen, B.F., Wu, C.H., Faltinsen, O.M., 2023. The mechanism of switching direction of swirling sloshing waves. J. Fluid Mech. 954 (A2).

Colagrossi, A., Antuono, M., Le Touzé, D., 2009. Theoretical considerations on the free-surface role in the smoothed-particle-hydrodynamics model. Phys. Rev. E 79, 056701.

Colagrossi, A., Antuono, M., Souto-Iglesias, A., Le Touzé, D., 2011. Theoretical analysis and numerical verification of the consistency of viscous smoothed-particle-hydrodynamics formulations in simulating free-surface flows. Phys. Rev. E 84, 026705.

Colagrossi, A., Bouscasse, B., Marrone, S., 2015. Energy-decomposition analysis for viscous free-surface flows. Phys. Rev. E 92, 053003.

Di Mascio, A., Antuono, M., Colagrossi, A., Marrone, S., 2017. Smoothed particle hydrodynamics method from a large eddy simulation perspective. Phys. Fluids 29, 035102.

Faltinsen, O.M., Lagodzinskyi, O.E., Timokha, A.N., 2020. Resonant three-dimensional nonlinear sloshing in a square base basin. part 5. three-dimensional non-parametric tank forcing. J. Fluid Mech. 894, A10.

Faltinsen, O.M., Rognebakke, O.F., Timokha, A.N., 2003. Resonant three-dimensional nonlinear sloshing in a square-base basin. J. Fluid Mech. 487, 1–42.

Faltinsen, O., Rognebakke, O., Timokha, A., 2005a. Classification of three-dimensional nonlinear sloshing in a square-base tank with finite depth. J. Fluids Struct. 20, 81–103.

Faltinsen, O.M., Rognebakke, O.F., Timokha, A.N., 2005b. Resonant three-dimensional nonlinear sloshing in a square-base basin. part 2. effect of higher modes. J. Fluid Mech. 523, 199–218.
Faltinsen, O.M., Rognebakke, O.F., Timokha, A.N., 2006. Resonant three-dimensional nonlinear sloshing in a square-base basin. part 3. base ratio perturbations. J. Fluid Mech. 551, 93–116.
Faltinsen, O.M., Timokha, A.N., 2009. Sloshing. Volume 577. Cambridge University Press, Cambridge.
Faltinsen, O.M., Timokha, A.N., 2017. Resonant three-dimensional nonlinear sloshing in a square-base basin. part 4. oblique forcing and linear viscous damping. J. Fluid Mech. 822, 139–169.
Jin, X., Tang, J., Tang, X., Mi, S., Wu, J., Liu, M., Huang, Z., 2020. Effect of viscosity on sloshing in a rectangular tank with intermediate liquid depth. Exp. Therm Fluid Sci. 118, 110148.
Lind, S., Xu, R., Stansby, P., Rogers, B., 2012. Incompressible smoothed particle hydrodynamics for free-surface flows: A generalised diffusion-based algorithm for stability and validations for impulsive flows and propagating waves. J. Comput. Phys. 231, 1499–1523.
Liu, D., Lin, P., 2008. A numerical study of three-dimensional liquid sloshing in tanks. J. Comput. Phys. 227, 3921–3939.
Lo, E.Y., Shao, S., 2002. Simulation of near-shore solitary wave mechanics by an incompressible SPH method. Appl. Ocean Res. 24, 275–286.
Macia, F., Antuono, M., González-Gutiérriez, L.M., Colagrossi, A., 2011. Theoretical analysis of the no-slip boundary condition enforcement in SPH methods. Progr. Theoret. Phys. 125, 1091–1121.
Malan, L.C., Pilloton, C., Colagrossi, A., Malan, A.G., 2022. Numerical calculation of slosh dissipation. Appl. Sci. 12 (12390).
Marcotte, A., Gallaire, F., Bongarzone, A., 2023. Swirling against the forcing: evidence of counter-directed sloshing waves in orbital-shaken reservoirs. arXiv preprint arXiv:2302.14579.
Marrone, S., Colagrossi, A., Calderon-Sanchez, J., Martinez-Carrascal, J., 2021a. Numerical study on the dissipation mechanisms in sloshing flows induced by violent and high-frequency accelerations. II. comparison against experimental data. Phys. Rev. Fluids 6, 114802.
Marrone, S., Colagrossi, A., Gambioli, F., González-Gutiérrez, L., 2021b. Numerical study on the dissipation mechanisms in sloshing flows induced by violent and high-frequency accelerations. I. theoretical formulation and numerical investigation. Phys. Rev. Fluids 6, 114801.
Marrone, S., Saltari, F., Michel, J., Mastroddi, F., 2023. SPH modelling of dissipative sloshing flows under violent vertical harmonic excitation. J. Fluids Struct. 119, 103877.
Meringolo, D., Marrone, S., Colagrossi, A., Liu, Y., 2019. A dynamic δ-SPH model: How to get rid of diffusive parameter tuning. Comput. & Fluids 179, 334–355.
Michel, J., Antuono, M., Oger, G., Marrone, S., 2023. Energy balance in quasi-lagrangian Riemann-based SPH schemes. Comput. Methods Appl. Mech. Engrg. 410, 116015.
Michel, J., Durante, D., Colagrossi, A., Marrone, S., 2022. Energy dissipation in violent three-dimensional sloshing flows induced by high-frequency vertical accelerations. Phys. Fluids 34, 102114.
Monaghan, J.J., 2005. Smoothed particle hydrodynamics. Rep. Progr. Phys. 68 (1703).
Nestor, R.M., Basa, M., Lastiwka, M., Quinlan, N.J., 2009. Extension of the finite volume particle method to viscous flow. J. Comput. Phys. 228, 1733–1749.
Oger, G., Marrone, S., Le Touzé, D., De Leffe, M., 2016. SPH accuracy improvement through the combination of a quasi-Lagrangian shifting transport velocity and consistent ALE formalisms. J. Comput. Phys. 313, 76–98.
Pilloton, C., Bardazzi, A., Colagrossi, A., Marrone, S., 2022. SPH method for long-time simulations of sloshing flows in LNG tanks. Eur. J. Mech. B Fluids 93, 65–92.
Quinlan, N., Lastiwka, M., Basa, M., 2006. Truncation error in mesh-free particle methods. Internat. J. Numer. Methods Engrg. 66, 2064–2085.
Rogers, B.D., Dalrymple, R.A., 2005. SPH modeling of breaking waves. In: Coastal Engineering 2004: (in 4 Volumes). World Scientific, pp. 415–427.
Saltari, F., Pizzoli, M., Coppotelli, G., Gambioli, F., Cooper, J.E., Mastroddi, F., 2022. Experimental characterisation of sloshing tank dissipative behaviour in vertical harmonic excitation. J. Fluids Struct. 109, 103478.
Smagorinsky, J., 1963. General circulation experiments with the primitive equations: I. the basic experiment. Mon. Weather Rev. 91, 99–164.
Tsarau, A., Lugni, C., Lucarelli, A., Kristiansen, D., Lader, P., 2021. Sloshing in a rotating liquid inside a closed sea cage for fish farming. Phys. Fluids 33, 037114.
Van Driest, E.R., 1956. On turbulent flow near a wall. J. Aeronaut. Sci. 23, 1007–1011.
Wendland, H., 1995. Piecewise polynomial, positive definite and compactly supported radial functions of minimal degree. Adv. Comput. Math. 4, 389–396.
Wu, C.H., Chen, B.F., 2009. Sloshing waves and resonance modes of fluid in a 3d tank by a time-independent finite difference method. Ocean Eng. 36, 500–510.
Wu, C.H., Chen, B.F., Hung, T.K., 2013. Hydrodynamic forces induced by transient sloshing in a 3d rectangular tank due to oblique horizontal excitation. Comput. Math. Appl. 65, 1163–1186.
Wu, C.H., Hung, T.K., Chen, B.F., 2023. Kinematic, dynamic and energy characteristics of swirling sloshing waves. Ocean Eng. 272, 113875.